HEALTH AND MEDICINE

Biophysical and biomolecular interactions of malaria-infected erythrocytes in engineered human capillaries

Christopher Arakawa[1]*, Celina Gunnarsson[1]*, Caitlin Howard[1]*, Maria Bernabeu[2]*, Kiet Phong[1], Eric Yang[1], Cole A. DeForest[1,3†], Joseph D. Smith[2,4†], Ying Zheng[1†]

Microcirculatory obstruction is a hallmark of severe malaria, but mechanisms of parasite sequestration are only partially understood. Here, we developed a robust three-dimensional microvessel model that mimics the arteriole-capillary-venule (ACV) transition consisting of a narrow 5- to 10-μm-diameter capillary region flanked by arteriole- or venule-sized vessels. Using this platform, we investigated red blood cell (RBC) transit at the single cell and at physiological hematocrits. We showed normal RBCs deformed via in vivo–like stretching and tumbling with negligible interactions with the vessel wall. By comparison, *Plasmodium falciparum*–infected RBCs exhibited virtually no deformation and rapidly accumulated in the capillary-sized region. Comparison of wild-type parasites to those lacking either cytoadhesion ligands or membrane-stiffening knobs showed highly distinctive spatial and temporal kinetics of accumulation, linked to velocity transition in ACVs. Our findings shed light on mechanisms of microcirculatory obstruction in malaria and establish a new platform to study hematologic and microvascular diseases.

INTRODUCTION

Microcirculatory disorders are associated with both infectious and noninfectious diseases, including *Plasmodium falciparum* malaria (*1*), sickle cell disease (*2*), and type 2 diabetes (*3*). Sequestration of *P. falciparum*–infected red blood cells (IRBCs) in the microcirculation has been recognized as a critical event in severe malaria pathogenesis and associated life-threatening complications, leading to approximately 500,000 deaths per year (*4*, *5*). During the blood stage of infection, *P. falciparum* parasites extensively modify the host erythrocyte cytoskeleton and membrane, resulting in altered red blood cell (RBC) deformability and new adhesive properties. In particular, IRBCs display knob-like surface protrusions that stiffen the erythrocyte membrane (*6*, *7*) and present the *P. falciparum* erythrocyte membrane protein 1 (PfEMP1) ligands that mediate cytoadhesion to the vascular endothelium (*8*, *9*). Both knobs and PfEMP1 are thought to contribute to IRBC sequestration, giving rise to enhanced disease severity through small vessel occlusion, tissue ischemia, and eventual organ failure (*1*, *8*, *10*–*13*). In addition, sequestered IRBCs may localize host or parasite-derived products that contribute to endothelial dysfunction and organ damage (*14*). Worldwide deaths attributed to malaria remain high, even after the introduction of more effective, faster-acting, antimalaria drugs (*15*). Investigating disease mechanisms and new therapeutic approaches to combine with antimalaria drugs has proven challenging as *P. falciparum* is a human tropic pathogen with complications focused at the capillary and postcapillary venule (*16*, *17*). As no proper in vitro human capillary model exists, inferences must instead be drawn from postmortem analysis or studies in non-natural hosts [primate infections (*18*) or ex vivo rat microcirculatory models (*12*)], in which host receptors are not the natural binding partners for *P. falciparum* ligands.

Within the microcirculation, RBCs (diameter d_{AVG} = 7.5 μm) deform as they traverse capillaries (d_{AVG} = 3 to 10 μm) that are often narrower than their resting-state diameters. To understand how the altered deformability of *P. falciparum*–IRBCs contributes to microcirculatory obstruction, the mechanics of RBC flow have been modeled in vitro using narrow glass tubes or wedge-shaped, rigid PDMS (polydimethylsiloxane)–based microfluidic devices (*19*–*24*). While these approaches have demonstrated geometric thresholds for mechanical trapping of IRBCs (*20*, *25*), they do not account for either the lubricating properties of the endothelial glycocalyx or the adhesive contributions of endothelial cells (*26*, *27*). Conversely, flow-based, endothelial monolayer models have investigated the role of different host receptors in parasite cytoadhesion (*28*–*30*), yet they are unable to capture the geometric constraints that govern IRBC flow through narrow capillary constrictions or the flow rate transitions encountered as cells traverse different-size microvessels. The altered adhesive and mechanical properties of IRBCs and the alterations in flow dynamics experienced by IRBCs within microvessels likely all contribute to sequestration in a mutually dependent manner. Without an adequate human capillary model, the contributions of these biophysical and biochemical factors of IRBC sequestration cannot be explored.

We addressed these challenges by developing a three-dimensional (3D) arteriole-capillary-venule (ACV) microvessel unit, in which endothelial cells are grown in a native extracellular matrix. After optimizing the design parameters of 3D capillary fabrication and endothelialization, we used the ACV unit to identify the distinct spatiotemporal dynamics of RBC capillary transit and dissect the individual contributions of cytoadhesion and mechanical stiffening to IRBC sequestration. Our study sheds light on the mechanisms underlying IRBC sequestration during severe malaria infection and provides a unique platform to study the cellular, microfluidic, and geometric factors that give rise to microvascular obstruction in hematologic diseases.

---

[1] Department of Bioengineering, University of Washington, Seattle, WA 98105, USA. [2] Seattle Children's Research Institute, Seattle, WA 98101, USA. [3] Department of Chemical Engineering, University of Washington, Seattle, WA 98195, USA. [4] Department of Global Health, University of Washington, Seattle, WA 98105, USA.
*These authors contributed equally to this work.
†Corresponding author. Email: yingzy@uw.edu (Y.Z.); joe.smith@seattlechildrens.org (J.D.S.); profcole@uw.edu (C.A.D.)

RESULTS

Generation of perfusable capillary microchannels via collagen photoablation

To create an efficient capillary model, we first fabricated an acellular 3D ACV microvessel unit via a two-step process. First, large arteriole or venule-sized microchannels (lumen diameter d = 200 μm, spaced 450 μm apart) were lithographically fabricated in collagen hydrogels (7.5 mg/ml, ~200 to 500 Pa), as previously described (*31*). Then, an array of capillary-sized microchannels or features of arbitrary user-defined geometries (*32*) were generated between the two main channels using multiphoton microscopy–guided femtosecond laser photoablation (fig. S1A). Ablated regions were confirmed using second harmonic imaging of collagen fibers (fig. S1B). Arrays of channels ranging from 5 to 20 μm in diameter were rapidly produced (~75 channels/hour) with high density and robust perfusability by 0.22-μm fluorescent beads (fig. S1, C and D). The density generated (~11,600 channels/mm^2 for 5-μm arrays; fig. S1D) can reach a similar or higher level than that observed in the human heart [1100 capillaries/mm^2 in vivo; (*33*)].

Endothelialization of this ACV model posed substantial challenges as conventional methods of cell seeding after microvessel fabrication (*31*) led to sparse endothelial coverage within the microchannel arrays and nonperfusable vessels even after 7 days of culture. Successful endothelialization was achieved by leveraging the precise yet destructive nature of photoablation to simultaneously incur local endothelial cell injury while generating capillary-sized void spaces between two preformed main microvessels (Fig. 1A). This methodology encouraged endothelial cell migration and ingrowth into the ablated channels (Fig. 1B). Stable endothelial coverage was observed in the capillary-sized channels as early as 18 hours following photoablation (Fig. 1C and movie S1), and complete endothelialization of 20-μm channels was observed after 4 days of culture under gravity-driven flow across the microvessels (Fig. 1B).

Photoablation-guided cellular ingrowth establishes robust capillaries in an ACV unit

In vivo, capillary lengths range from 150 to 500 μm (*34*). To determine the vessel patency at high vessel density, 2 × 2 arrays of straight channels, consisting of either 10- or 20-μm lumen diameters spaced 5, 10, or 20 μm apart, were photoablated between two preformed main microvessels of 200-μm diameter (fig. S2). Microchannels that were initially separated by only 5 or 10 μm demonstrated partial or complete fusion after endothelial cell ingrowth from the two main microvessels, leading to a larger vessel diameter (fig. S2, B and C). By comparison, microchannels of 20-μm diameter separated by a 20-μm distance maintained high vessel diameter fidelity (Fig. 1B and fig. S2C), Whereas 10-μm diameter channels exhibited incomplete endothelialization and patchy endothelial coverage (fig. S2B), vascularization was more efficient in 20-μm channels. The average length of continuous endothelium in 10-μm diameter channels was approximately 126.7 ± 60.2 μm, corresponding to an aspect ratio [AR = length (l): lumen diameter (d) of 12.7 ± 6.0] (fig. S2D). In contrast, 20-μm-diameter vessels demonstrated near-complete endothelialization (365 ± 105.4 μm) (AR = 18.3 ± 5.3). Moreover, 20-μm-diameter vessels exhibited clear lumens upon histological staining and deposited abundant type IV collagen, suggesting the generation of a robust basement membrane (Fig. 1, D and E). Together, these data suggest geometric constraints for small vessel size formation (a minimum distance of 20 μm between two parallel small channels and maximum AR of approximately 12 to 18) to maintain vessel patency, which has consistent range with human in vivo measurements for the length-to-diameter ratio (*33*).

In vivo, RBCs experience changes in velocity as they traverse different-sized microvessels within the ACV unit (*35*). To build a robust capillary model at smaller diameters (5 to 10 μm) that more accurately mimics the in vivo vascular tree, we designed a constriction-shaped ACV geometry with a gradual change of diameter and a reduced AR for the capillary regions. This design consisted of five distinct regions that combine to form a symmetric hourglass shape: a precapillary arteriole and a postcapillary venule mimicking vessels with constant width (w = 40 μm, l = 80 μm, thereby AR = 2), which were connected to a capillary-sized region (w = 5 μm, l = 80 μm, AR = 16) by two flanking narrowing/expanding transition regions (w = 40 to 5 μm, l = 105 μm). This vessel design decreased the length of the capillary-sized region and increased the width or diameter of the sections that connected with the two main larger-sized microvessels, therefore promoting endothelial cell ingrowth and capillary patency (Fig. 1, F to J).

Two cell seeding approaches were tested for endothelialization efficiency and perfusability: (i) direct cell seeding of fully acellular channels followed by 7 days of culture and (ii) photoablation-guided capillary ingrowth for 4 days from two large preformed main vessels after 3 days of culture (7 days total). The hourglass-shaped ACV unit design supported robust endothelial cell ingrowth throughout the capillary-sized channels using both seeding approaches (fig. S3, A to D). While successful endothelialization could be achieved using either of the seeding methods (65 ± 1% versus 77 ± 7%, mean ± SEM), the percentage of perfusable capillaries was significantly higher when endothelial cells grew into the photoablated channels from preformed microvessels (57 ± 12% versus 17 ± 7%, mean ± SEM, $^{**}P < 0.002$) (fig. S3E). Implementation of photoablation-guided capillary ingrowth resulted in robust, consistent, and perfusable capillary-sized microvessels of 5- to 10-μm diameter, measured via confocal microscopy (Fig 1, F to J, and fig. S3, A and B). Similar to the two main vessels, the endothelium within the ACV regions was positive for vascular endothelial (VE)–cadherin (a marker of intercellular junctions) and von Willebrand factor (a marker of Weibel-Palade bodies) (Fig. 1, F to J). We further measured the diameter at the narrowest region of the capillary constriction zones, which ranged from 7.5 to 13.6 μm (10.9 ± 1.8 μm, mean ± SD, n = 25 capillaries) in confocal microscopy and 5.6 to 13.2 μm (8.6 ± 2.1 μm, mean ± SD, n = 15 capillaries) in two-photon microscopy.

Electron microscopic analysis confirmed the gradual changes of vessel diameter along the longitudinal direction (Fig. 1, G to I, and fig. S4). Ultrastructure of vessel regions with cross-sectional diameters larger than 20 μm was often formed from two or more endothelial cells, connected with focal contacts and junctions between surrounding cells (Fig. 1, G1 and G2). By comparison, at regions of 10 μm or smaller in diameter, lumens appeared to be enclosed by a single endothelial cell, which formed extensive focal contacts and complex junctions with overlapping cell peripherals from one or two neighboring cells (Fig. 1, G3). The lumenal wall displayed heterogeneous thickness, ranging from approximately 100 nm to several micrometers at the regions of cell bodies or overlapping cell regions. This also led to varying vessel diameters in both longitudinal and circumferential directions across the ACV unit, although vessels remained intact and continuous across almost all planes examined (Fig. 1, G and H, and fig. S4). Together, our data suggest an efficient approach to fabricate a

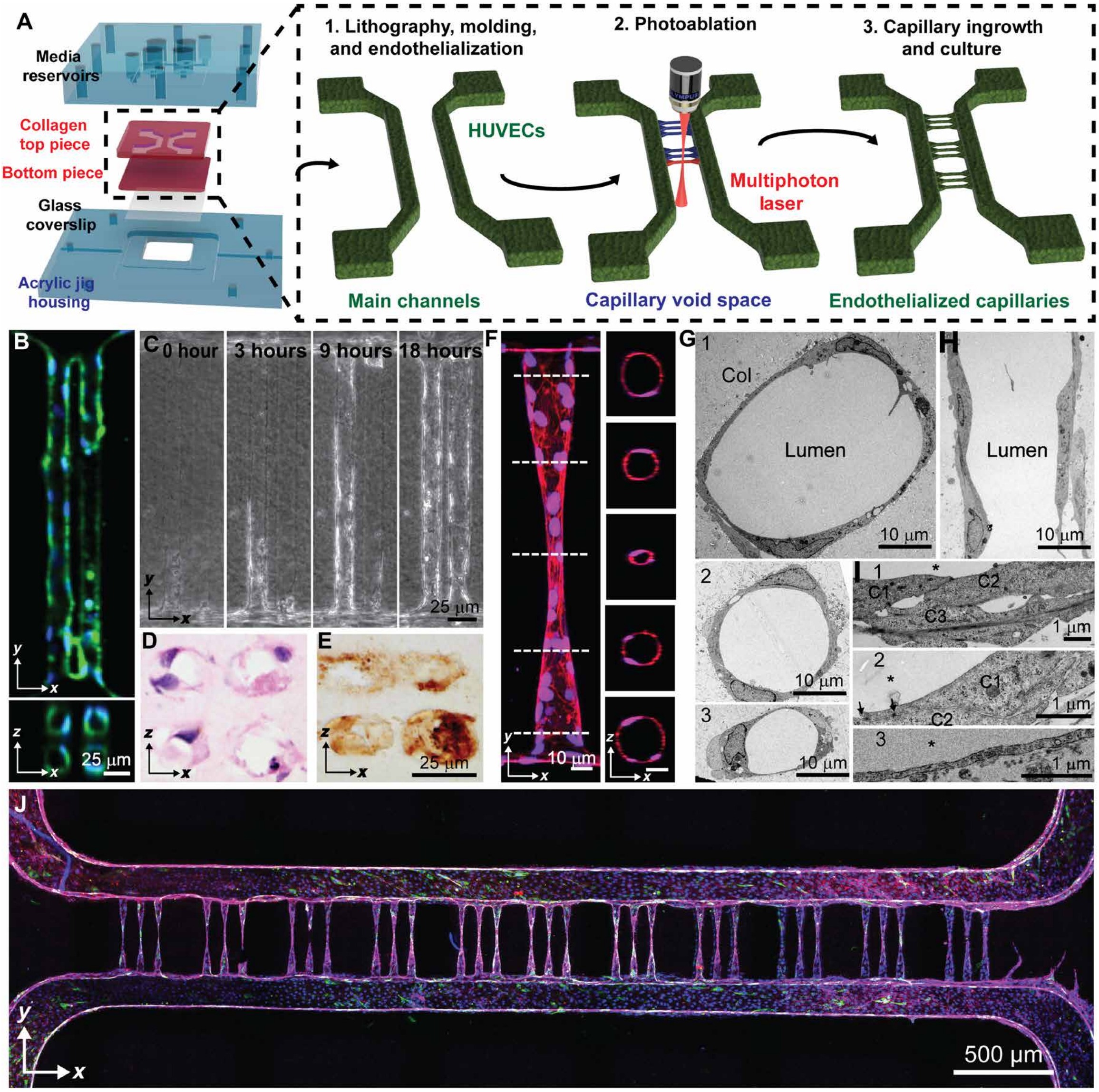

Fig. 1. Photoablation-guided capillary growth in lithography-based microvessel devices. (**A**) Diagram of device assembly and capillary fabrication. Main channels were generated by soft lithography in acrylic jigs followed by capillary generation by photoablation and endothelial ingrowth. (**B**) Array (2 × 2) of 20-μm-diameter vessels demonstrates stable vessel lumens. Green: F-actin; blue: nuclei. (**C**) Endothelial ingrowth over 18 hours demonstrates complete vessel formation. (**D** and **E**) Cryosectioned capillaries were stained with (D) hematoxylin and eosin as well as (E) type IV collagen, demonstrating lumen formation by single endothelial cells and robust basement membrane deposition. (**F**) Constriction vessel design allows for the generation of sub–10-μm-diameter capillaries shown in both projected and cross-sectional views. Red: VE-cadherin; blue: nuclei. (**G** to **I**) Ultrastructural analysis of capillary vessel regions by transmission electron microscopy (TEM) shows vessels at varying diameters (from 40 to 10 μm) in cross-sectional (G and I) and longitudinal (H) views and varying wall thicknesses and junctions at cell-cell contact in zoomed views (I). Cross-sectional views of vessel regions near the connection. Col: collagen substrate; *: lumen; C: cells. (**J**) Stitched confocal image demonstrates complete vessel network consisting of 33 capillaries. Green: von Willebrand factor; blue: nuclei; red: VE-cadherin; purple: F-actin.

continuous, endothelialized, perfusable ACV unit with high fidelity and patency.

Normal and infected RBCs display different mechanics of motion and deformation across the capillary region

When normal RBCs were perfused through the completely endothelialized ACV devices at full hematocrit, the presence of endothelium appeared to facilitate the smooth perfusion of RBCs through the capillary constriction region (movie S2). By comparison, in acellular collagen microchannels with the same hourglass geometry, RBCs accumulated upstream before entering the narrowest region, leading to local increases of hematocrit, as well as intermittent jetting of RBCs into the capillary constriction zones and much lower hematocrit further downstream (movie S3). This comparison of acellular and endothelialized microvessels reinforces the importance of the endothelium in understanding the interaction of RBCs and capillaries.

We next exploited this endothelialized capillary model to study the biomechanical and functional differences between normal and infected RBCs under flow. To allow visualization of individual cells as they traverse the ACV units, RBCs were perfused at a low hematocrit.

When normal RBCs were perfused through ACVs at low hematocrit and velocities similar to in vivo capillary flow rates (≈250 to 1500 μm/s) (*34*, *36*), they displayed in vivo–like stretching in the capillary region and tumbling behavior in the pre- and postcapillary regions (Fig. 2, A and B, and movies S4 and S5). Normal RBCs readily traversed the capillary regions down to 5 μm in diameter and assumed a variety of deformations, including parachute-like, slipper-like, and discocyte shapes (Fig. 2C), in agreement with previous in vivo observations (*19*), computational simulations (*37*, *38*), and microfluidic studies in narrow glass tubes (*38*). Using edge detection–based image analysis (see the Supplementary Materials and Methods and fig. S5), we tracked the position, velocity, shape, and orientation of individual RBCs throughout the capillaries (Fig. 2D). Normal RBCs showed two major modes of motion in the capillary regions: elongation, characterized by stretching along the major axis by up to twofold (Fig. 2D (i) and movie S4), and tumbling, characterized by oscillations in major axis orientation (Fig. 2D (ii) and movie S5). Compared with normal RBCs, *P. falciparum*–IRBCs present increased rigidity due to knob-like modifications to the erythrocyte cytoskeleton (*6*, *7*) and modest changes in RBC volume and its biconcave shape due to the growing

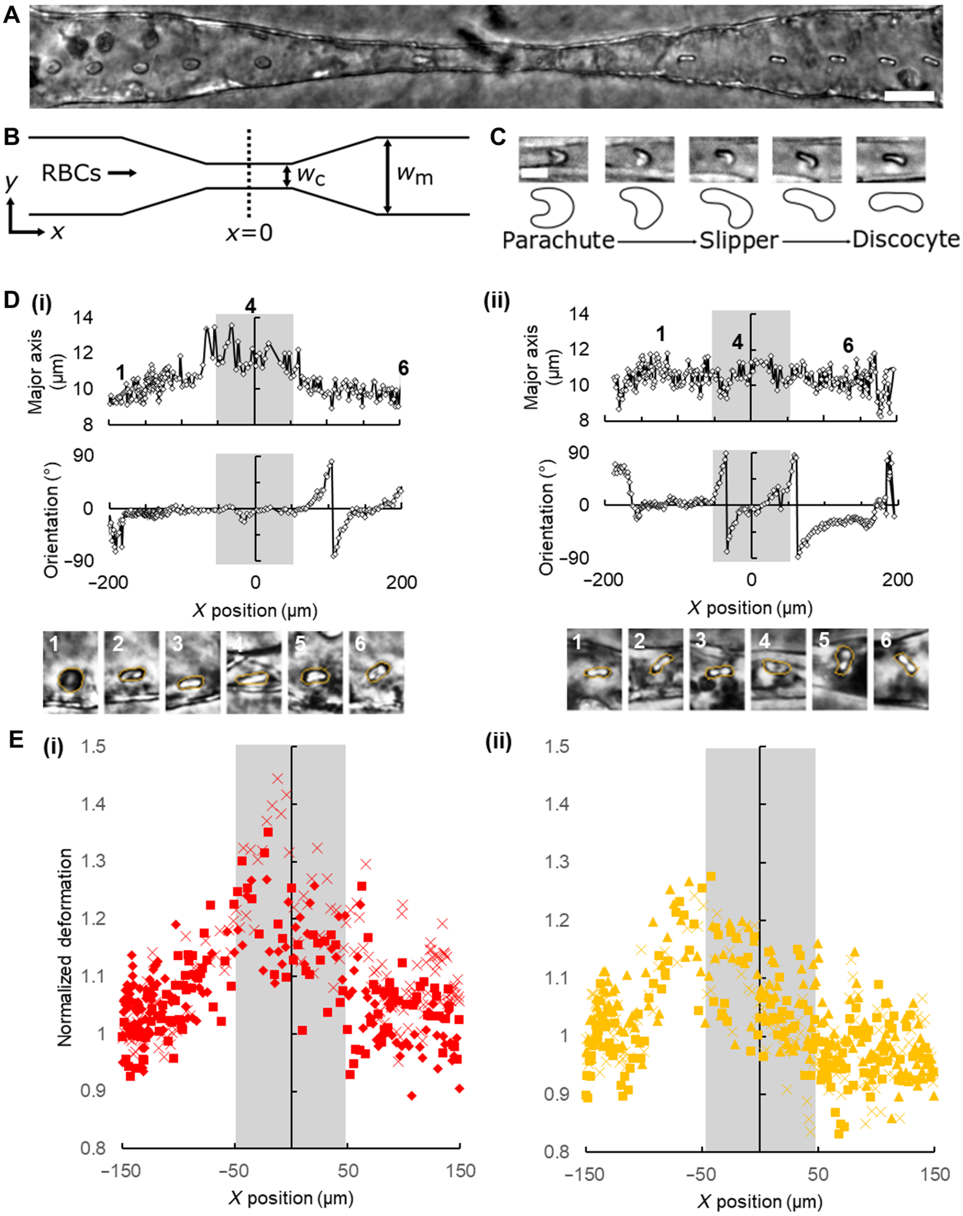

Fig. 2. Motion and deformation of RBCs while traversing capillary constriction zones. (**A**) Superimposed time lapse image series of RBC motion through an endothelialized vessel. Time lapse interval: 0.1 s. Scale bar, 25 μm. (**B**) Schematic showing RBC perfusion through constriction-shaped vessel. $w_c = 10$ μm; $w_m = 40$ μm. (**C**) Representative examples of parachute-, slipper-, and discocyte-like RBC deformations in capillary constrictions. Scale bar, 10 μm. (**D**) Representative traces of RBC major axis length and orientation for (i) stretching and (ii) tumbling RBCs, where $x = 0$, $y = 0$ is the center of the capillary; gray boxes: capillary extents. (**E**) Normalized extent of deformation, defined as the ratio of major axis length at a given position to the average major axis length in the precapillary region for (i) normal RBCs and (ii) knobless malaria-IRBCs ($n = 3$; each biological replicate is represented by one symbol, ■, ♦, ×, or ▲).

intracellular parasite (*39*), which might change the IRBC mechanics through capillary-sized vessels. To understand how the intracellular parasite body contributes to the biomechanics of IRBC traversal through the microcirculation, independently of knob rigidification and cytoadhesion, we perfused a clonally derived parasite variant called 2G2 (fig. S6), which has been selected for lack of knobs by gelatin (*40*). Although not statistically different compared with normal RBCs, 2G2-IRBCs presented minimal elongation and mostly tumbled through the capillary region despite being perfused at similar velocities to normal RBCs (Fig. 2E and movie S6). Because rolling and tumbling along the microvascular endothelium enhance cytoadhesion and increase the probability of ligand-receptor interaction at high shear stress (*41*), we expect that these differences in tumbling motion may enhance the ability of malaria-infected RBCs to both be mechanically trapped and cytoadhere in capillaries.

P. falciparum–IRBCs occlude the capillary region at physiological hematocrit conditions

In the microcirculation, hydrodynamic forces encourage separation and margination of IRBCs from their uninfected RBC counterparts toward the vessel wall, enhancing cytoadhesive interactions with endothelial cells (*42*, *43*). To investigate whether IRBCs sequester at physiological hematocrit concentrations (Fig. 3A), fluorescently labeled IRBCs (0.4 to 4% parasitemia) or normal RBCs were perfused at 40% hematocrit using gravity-driven flow, leading to an average flow rate at approximately 0.002 μl/min in each capillary during the first 30 min of perfusion. The cell accumulation was assessed at 1, 4, 7, and 20 min by fluorescence imaging and was compared with flow modeling to relate predicted flow dynamic changes across the microvessels to retention and occlusion events (Fig. 3, B and C). Normal RBCs traversed the entire constriction zone with minimal sequestration in any vessel region (Fig. 3, C to I, and movie S7). Both labeled and unlabeled normal RBCs deformed as necessary to pass through the narrowest regions, suggesting that the membrane-labeling procedure did not significantly increase sequestration potential. By comparison, IT4VAR19, a knob-positive (K^+) and cytoadherent parasite variant ($PfEMP1^+$) (fig. S6) (*44*) displayed steady accumulation (Fig. 3C (ii) and movie S8). Kinetic video analysis demonstrated sequestration throughout the capillary constriction zone with highest accumulation in the first half. Complete occlusion of the capillary region could be observed within minutes after initiation of flow, followed by accumulation of fluorescent IRBCs upstream of the blockage. At end point, $K^+PfEMP1^+$ IRBCs demonstrated high fluorescent signals centered in the capillary region and extending into the post- and precapillary regions. Ultrastructural analysis showed that the capillary regions contained a mixture of both infected and normal RBCs (fig. S7, A and B), suggesting that occluded vessels may trap normal RBCs. By transmission electron microscopy (TEM), IRBCs were found in close apposition to lumenal walls, even following perfusion washing (fig. S7). Moreover, some IRBCs were trapped or encircled by the endothelial cell membranes (fig. S7) or appeared to have been fully engulfed by an endothelial cell (fig. S7B), as observed previously in monolayer assays with immortalized endothelial cells (*45*).

Parasite-induced knobs and cytoadhesion ligands make independent and distinct contributions to *P. falciparum*–IRBC accumulation in capillary regions

To elucidate the relative contributions of altered adhesive and mechanical properties in IRBC microvessel obstruction, we trypsinized IT4VAR19 IRBCs to remove the surface presentation of PfEMP1s while leaving the knobs intact ($K^+PfEMP1^-$) (fig. S8). Previous work by atomic force microscopy has established that *P. falciparum* knobs are unaffected by trypsin treatment (*46*). Following trypsinization, there was a marked loss of antibody recognition with two polyclonal antibody reagents against the first and fourth DBL domains in the IT4VAR19 PfEMP1 variant (fig. S8). Perfusion of $K^+PfEMP1^-$ IRBCs demonstrated minimal sequestration throughout the constriction zone, with binding levels similar to normal RBCs in all vessel regions (Fig. 3, C to E, and movie S9). These findings suggest that while mechanical stiffening may contribute to IRBC margination toward the vessel wall in the postcapillary regions (*43*), surface-active PfEMP1 is necessary to cause IRBC sequestration. Furthermore, despite the geometric confinement in capillaries, mechanical stiffening on its own is insufficient to induce the same trapping in the 5- to 10-μm capillary-sized constrictions observed with the $K^+PfEMP1^+$ IRBCs.

We next perfused 2G2 (K^-) to better understand the contribution of knobs to cytoadhesion (*40*), as they are thought to enhance PfEMP1-mediated adhesion (*9*, *12*, *47*) and increase the mechanical stiffening of IRBCs (*48*). Notably, both IT4VAR19 and 2G2 express endothelial protein C receptor (EPCR)–binding *var* transcripts (*49*), but 2G2 exhibits much weaker cytoadhesive capabilities under flow conditions (*50*). Although the weakly adherent 2G2 parasites (K^-) exhibited higher sequestration rates than the trypsinized IT4VAR19 ($K^+PfEMP1^-$), cell accumulation was concentrated to the second half of the capillary constriction zone, where cells would experience deacceleration and less flow shear as they transition into the larger-diameter region (Fig. 3, C and D, and movie S10). Together, this analysis identifies distinct and independent contributions of the microcirculatory hemodynamics and parasite-induced modifications to RBCs in microvascular obstruction.

DISCUSSION

Cytoadhesion of *P. falciparum*–IRBCs is a major virulence determinant, but knowledge gaps exist in how parasites cause microvascular obstruction, and the ability to study important human microcirculatory disorders in vitro has been limited to nondeformable glass or microfluidic chamber platforms. Here, we describe an efficient fabrication approach for engineering robust and patent capillary arrays in an ACV unit. Our studies exploited this model to investigate normal and malaria-infected RBCs under perfusion and to identify sequential events of biomolecular and biophysical interactions between RBCs and capillary walls that led to parasite sequestration and microvascular occlusion.

Whereas normal RBCs readily traversed the narrow capillary constriction zones, *P. falciparum*–IRBCs rapidly accumulated in these regions. Our study identified distinct contributions of parasite-induced knobs and cytoadhesion ligands in cell accumulation by perfusing IRBCs with different knob structures and trypsinized IRBCs to preserve the knob structure while eliminating the cytoadhesion effects (*46*). Although trypsinized IRBCs with cleaved parasite cytoadhesion ligands exhibited limited accumulation in the capillary constriction regions, parasites lacking knobs accumulated at the capillary-venule transition where flow rates were deaccelerating. The efficient traversal of trypsinized IRBCs through narrow constrictions is consistent with previous microfluidic studies, which demonstrate mechanical trapping of IRBCs only in nondeformable channels below 4 μm in diameter (*20*). Knob membrane stiffening

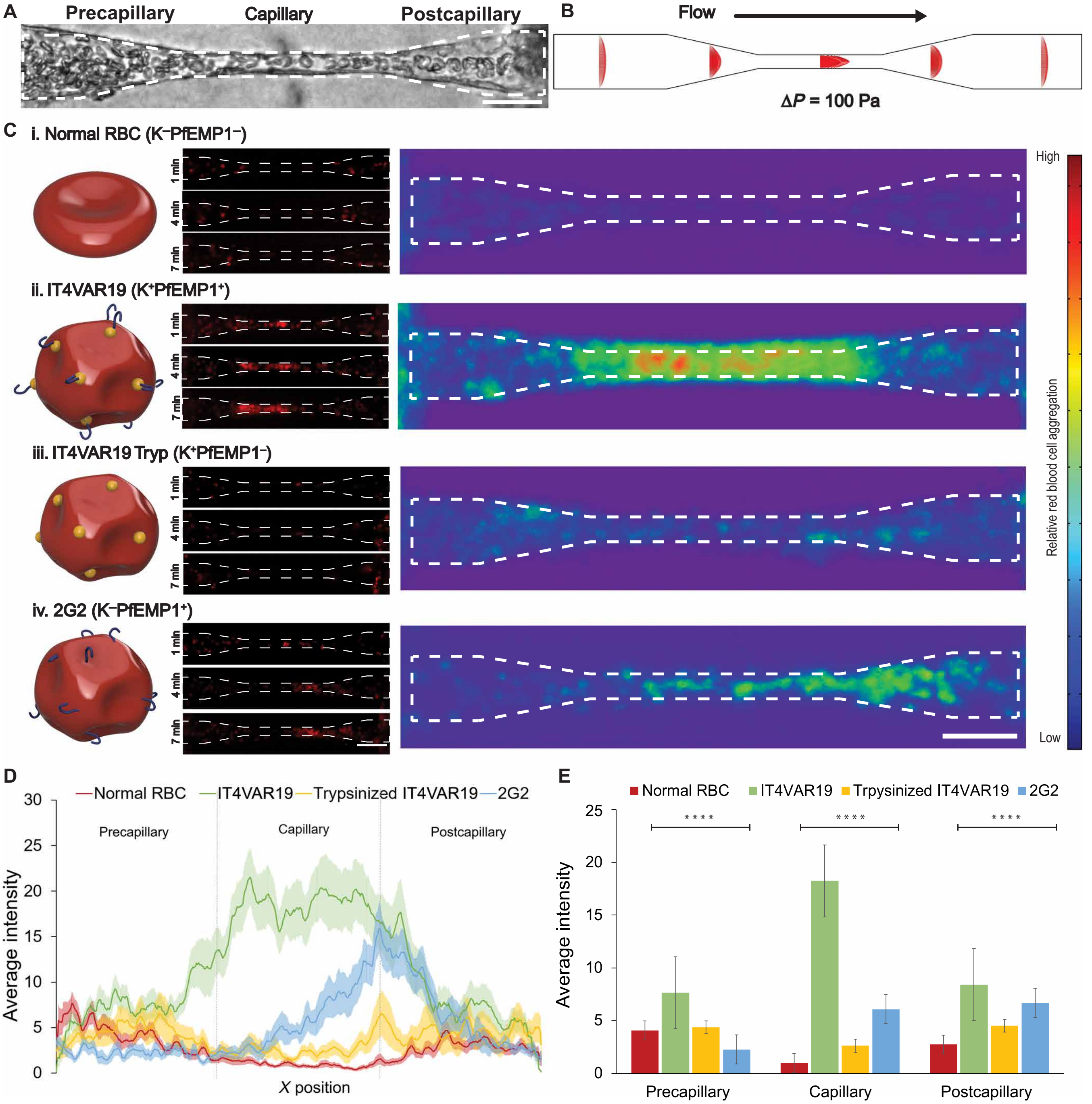

Fig. 3. Population dynamics analysis of RBC flow and accumulation within constriction capillaries. (**A**) Bright-field image of RBCs flowing through a constriction vessel. Dotted lines demonstrate capillary outline trace. (**B**) Flow velocity model of a single capillary based on fabrication dimensions. (**C**) Left: Schematic illustrations of the different types of perfused RBCs and IRBCs. Middle: Representative image of binding kinetics within the capillary constriction zones. IRBCs are shown in red. Right: Spatial distribution of accumulation after 20 min of perfusion represented by a combined heat map of average fluorescence from multiple experiments. Normal RBC ($n = 24$), IT4VAR19 ($n = 26$), trypsinized IT4VAR19 ($n = 19$), and 2G2 ($n = 19$). (**D** and **E**) Quantification of average intensity as a measure of x position (D) and comparison among precapillary, capillary, and postcapillary regions (E). $n = 24$, 26, 17, and 19 ACV units quantified from $N = 4$ independent experiments for each condition of perfusion: normal RBC, IT4VAR19, trypsinized IT4VAR19, and 2G2, respectively. Analysis of variance (ANOVA) $F = 11.61$, $P < 0.00001$ for precapillary region, ANOVA $F = 47.83$, $P < 0.00001$ for capillary region, and ANOVA $F = 6.41$, $P < 0.001$ for postcapillary region.

more likely contributes to splenic elimination, where interendothelial slits are as narrow as 3 μm (*51*, *52*). The knob-like protrusions anchor both the PfEMP1 cytoplasmic tail and erythrocyte cytoskeleton components, and previous work has established that they contribute to both parasite cytoadhesion strength (*9*) and the altered mechanical properties of *P. falciparum*–IRBCs (*48*) and thereby provide mechanical stability to the interactions between PfEMP1 and endothelial cells. In addition, by positioning the PfEMP1 cytoadhesion ligands above the cell body (*53*), knobs may also facilitate adhesion. With the distinct spatiotemporal binding of knobless parasites, our findings suggest that PfEMP1 physiological display in knobs facilitates IRBC capture from circulation, particularly in regions of higher flow shear in the capillary constriction area. This is consistent with previous work in ex vivo rat microcirculatory models and primate studies (*12*, *47*). Moreover, our findings reinforce the importance of cell deceleration and lower shear stress as cells exit from the capillaries, in mediating IRBC capture from flow. Postmortem autopsy studies have revealed higher IRBC accumulation rates at the postcapillary region (~3-fold increase as compared with precapillary regions) (*17*). Thus, our capillary model provides the means to dissect the interdependent interactions of microcirculatory hemodynamics and parasite modifications to malaria obstruction mechanisms.

The differences in pre- and postcapillary sequestration have been thought to arise from arterial-venous differences in flow rates or host receptor expression (*54*); nonetheless, this question has been difficult to study. In an ex vivo rat mesoappendix model, IRBC sequestration initiated in venules and sometimes extended upward by retrograde aggregation into the capillaries and arterioles (*12*). Although the rat mesoappendix model has been valuable to explore parameters influencing IRBC sequestration, recent work has also shown that severe malaria is linked to EPCR (*49*, *55*, *56*), which is highly divergent between humans and rats. Notably, both parasite lines used in this study (IT4VAR19 and 2G2) express EPCR-binding PfEMP1; thus, our human capillary constriction model has advantages in investigating the cytoadherence of severe malaria isolates in an in vitro human model.

A limitation of this model is the use of human umbilical cord endothelial cells (HUVECs), a cell type from large-vessel origin. However, HUVECs are commonly used to develop new 3D vascular platforms, and future studies can build on our design principles to incorporate different endothelial cells to develop organ-specific ACV units. In addition, the study of single-cell dynamics is challenging because of the lack of precise flow control in individual capillaries, owing to the parallel nature of many capillaries between the two main vessels in our system and the varying diameters in each capillary, similar to vessels found in vivo. Nevertheless, our ACV unit mimics physiological flow transitions within the microcirculation and could distinguish spatial and temporal binding differences between normal RBCs and IRBCs, as well as between wild-type parasites and parasites lacking PfEMP1 or the knob-like protrusions. Notably, parasite knob densities differ widely between fresh ex vivo parasites (*57*) and may also be modified in severe malaria infections (*58*), but it is unknown whether these variations modify IRBC cytoadhesion efficiency or influence disease severity. Our ACV model provides a fundamentally new approach to investigate microvascular obstruction in an in vitro human model. The success sheds light for future therapeutic development in treating blood-stage malaria and provides a potential platform for the studies of other microvascular disorders, such as sickle cell anemia, or in the context of transfusion medicine of blood products.

MATERIALS AND METHODS

Multiphoton ablation for the generation of acellular ACV unit

First, two parallel microchannels were fabricated via lithography and injection molding–based techniques in collagen gel, as described previously (*31*), to mimic arteriole- and venule-sized vessels. Next, multiphoton photoablation was performed in collagen gel between these two parallel microchannels using a Mai Tai DeepSee Ti:S laser (maximum power, 2.57 W) coupled with an Olympus FV1000MPE BX61 microscope fitted with a water immersion objective lens (25×, numerical aperture = 1.05). Microchannels and surrounding collagen regions were first identified by imaging of second-harmonic generation signals produced by collagen microfibers at excitation wavelength λ_{ex} = 860 nm and detection wavelength $\lambda_{detector}$ = 420 to 460 nm. Individual capillary-sized channels were designed within the collagen matrix by designating 3D regions of interest using the Olympus Fluoview software and then ablated by laser rastering (λ = 800 nm, I = 100%, pixel dwell time = 2 μs, 10 to 15 line repeat scans). Laser scanning in the X, Y, and Z dimensions were performed at ~1-μm step sizes. After the ablation, 0.22-μm-diameter fluorescent microbeads were perfused from one side of the main channels across the newly created capillary-sized channels to the other side at a pressure drop of 1 cmH$_2$O for 10 min, followed by imaging for evaluation of perfusability (fig. S1).

Endothelializing ACV unit

Two different procedures were investigated to form the endothelialized ACV units: (i) direct cell seeding of acellular channels and (ii) endothelial cell ingrowth after photoablation (figs. S2 and S3). In the first approach, the acellular ACV unit is first fabricated by photoablation, followed by seeding cells into the fully acellular device through the inlets of the two main parallel channels with 10-μl perfusions of HUVECs (Lonza, passages 3 to 7, with EBM basal medium supplemented with EGM endothelial cell growth medium) at a density of 8×10^6 cells/ml. Once the cells were attached, the devices were cultured under gravity-driven flow across the capillaries between the two main channels for 7 days. To create a gravity-driven flow, 200 and 180 μl of culture media was placed in the two main channel inlets to set the initial pressure drop at approximately 1 cmH$_2$O, leading to a peak velocity of approximately 1 mm/s across the ACV unit between the two main channels. The pressure drop was reset every 12 hours to maintain flow in the capillary regions.

In the second approach, the two main microchannels were first seeded with 10-μl perfusions of HUVECs at a density of 8×10^6 cells/ml and cultured for 3 days to form robust endothelialized lumens. Multiphoton photoablation was then performed to create microchannel void spaces that tapered down to 5 μm in diameter within the collagen scaffold between the lumenal wall of the two main vessels and ablate endothelial cells at the two end connections. Cellular and collagen ablation was confirmed by imaging identical areas after ablation using transmitted light and by second-harmonic generation imaging. The ablated vessels were then cultured for an additional 4 days to allow for endothelial cell ingrowth. The culture was maintained at the same pressure drop as the first approach and replenished twice a day with fresh culture media.

Parasite culture

P. falciparum parasite lines were cultured using anonymized human O$^+$ type RBCs (Valley Biomedical) in RPMI 1640 (Gibco) supplemented with 10% human type A$^+$ serum in a gas mixture of 90% N$_2$, 5% CO$_2$, and 5% O$_2$. The knobless parasite line 2G2 was previously derived by lack of gelatin floatation followed by limited dilution cloning (*40*), while the IT4VAR19 line was generated after repeatedly panning on transformed human brain microvascular endothelial cells followed by limited clonal dilution (*59*, *60*). Mature-stage IRBCs were enriched to 60 to 90% parasitemia by magnetic separation (MACS Cell Separator, LD Columns, Miltenyi Biotec) before perfusion for single-cell and population dynamics experiments. Both parasite lines predominantly express a single *var* gene and were derived from the IT4/FCR3 parasite genotype.

Monitoring RBC perfusion through capillaries at the single-cell scale

Magnetic enriched mature-stage *P. falciparum*–IRBCs or packed RBCs were resuspended in 10% fetal bovine serum (FBS)–containing EGM at 5×10^6 cells/ml, allowing the visualization of individual cells as they traverse the ACV devices. The dilute cell suspension was placed in the inlet and outlet of one microchannel at a maximum initial pressure drop of approximately 1 cmH_2O, creating a hydraulic gradient between the two microchannels and establishing gravity-driven flow across the capillaries. The peak velocity of the RBCs across the center capillary zone was approximately 1 mm/s. In single-cell dynamics studies, the pressure drop and resulting velocity rate were maintained and slightly adjusted over the course of the assay by removing or adding a small volume (~5 μl) of cell suspension from the inlet to maintain the RBC velocity in this range and allow for video capture of single-cell dynamics. The motion of individual RBCs within one of the capillary constriction channels was visualized with a Nikon TiE inverted widefield microscope, and videos were acquired at 20× and 250 to 500 frames/s using an Orca-Flash4.0V2 Digital CMOS camera (Hamamatsu). After acquisition, videos were analyzed using custom MATLAB scripts. For experiments with 2G2, videos were previously inspected, and only IRBCs with hemozoin were used in the downstream analysis. Briefly, individual frames containing RBCs were smoothed using a Wiener filter, inverted, then background subtracted using a mean filter. RBCs were detected by applying a Canny edge detection operator. Small gaps in RBC outlines were closed automatically using an edge-linking algorithm or manually (fig. S5). Individual RBC outlines were linked into trajectories based on displacement between outlines in different frames. Out-of-focus and overlapping RBCs were excluded from the analysis. Biological replicates were taken in at least two different days.

Monitoring RBC perfusion at physiological hematocrit

Magnetic enriched mature-stage *P. falciparum*–IRBCs or packed RBCs were fluorescently labeled according to the PKH26 Red Fluorescent Cell Linker Kit (Sigma-Aldrich). To simulate blood with physiological parasitemia, labeled cells (normal RBCs or IRBCs) were added to unlabeled normal RBCs at a final parasitemia of 0.4 to 4% (iRBC/total RBC) and then diluted to 40% hematocrit in EGM (containing 5% FBS). RBCs were encouraged to flow across the device driven by a pressure drop of approximately 1 cmH_2O for 20 min, leading to a peak velocity of approximately 1 mm/s, mimicking measured physiological velocities within the capillaries (*34*). The perfusion of RBCs was monitored and imaged at different fields of view (three capillary channels in each field of view) and continuous time frames. At the beginning of the perfusion, devices were quickly scanned to identify perfusable channels. Videos were taken for 10 s for each perfusable channel in the same order at each time point to determine the location and extent of binding after 1, 4, 7, and 20 min of perfusion. Each condition was repeated in independent days.

Population dynamics analysis

Quantification of population dynamics was performed on fluorescent images taken after 20 min of perfusion. Images were normalized between average background values and peak fluorescent intensity values, and a two-pixel radius median filter was used to remove speckle noise using MATLAB. Masks were manually drawn to outline individual capillary constriction channels using ImageJ. Average fluorescent intensity was calculated at each x position as the sum of intensity values across the y dimension divided by the diameter of the vessel at this position. The central point of each capillary region was determined, and the average intensity maps were lined up across all images at this central point.

Trypsin treatment and flow cytometric analysis

IT4VAR19 trophozoite-stage enriched IRBCs were treated with a trypsin (66.67 μg/ml; Sigma-Aldrich) solution in 1× phosphate-buffered saline for 30 min at 37°C, followed by an inhibition with an equal volume of FBS before perfusion of capillary devices. To determine PfEMP1 surface expression after trypsinization, an IT4VAR19 culture was incubated for 30 min at 37°C with a trypsin solution (10 μg/ml). Surface PfEMP1 was recognized with rat polyclonal antibodies against IT4VAR19 DBLα2 and DBLγ6 (1:10) for 30 min at 4°C, followed by an incubation with goat anti-rat immunoglobulin G–Alexa Fluor 488 (1:400, Molecular Probes) for 30 min. Infected erythrocytes (parasite nuclei) were detected with ethidium bromide (2 μg/ml; Invitrogen). Stained cells were washed in phosphate-buffered saline and analyzed on an LSRII fluorescence-activated cell sorter machine (BD Biosciences). Analysis was performed using FlowJo 10 (Tree Star Inc., Ashland, OR).

Statistical analysis

All results are presented as means ± SE and assumed to be distributed approximately normally. The sample number represents the number of microvessel devices (ACV units) fabricated and analyzed unless otherwise noted. Single variable analysis with two-tailed t test assuming unequal variance was used to determine statistical significance between two samples for analysis of perfusability and endothelialization efficiencies. Two-way analysis of variance (ANOVA) was used to determine significance in population dynamics data, followed by Dunnett's multiple comparisons test.

SUPPLEMENTARY MATERIALS

Supplementary material for this article is available at http://advances.sciencemag.org/cgi/content/full/6/3/eaay7243/DC1

Supplementary Materials and Methods

Fig. S1. Photoablation-guided fabrication of acellular capillary-sized microchannels.

Fig. S2. Cellular limitations of capillary fabrication.

Fig. S3. Endothelialization strategies for capillary network.

Fig. S4. Ultrastructural analysis of vessels at capillary regions across the ACV units imaged via TEM.

Fig. S5. Edge detection workflow for studying traversal of single RBCs through a capillary-sized constriction.

Fig. S6. Transcriptional profiling of *var* gene expression in the two parasite lines.

Fig. S7. Ultrastructural analysis of capillary region after perfusion of RBCs imaged via TEM.

Fig. S8. Trypsin cleaves the surface-expressed IT4VAR19 PfEMP1 variant.

Movie S1. Endothelial ingrowth into 20-μm capillaries between two large vessels after photoablation.

Movie S2. Representative video of normal RBCs perfused through endothelialized capillaries at physiological hematocrit.

Movie S3. Representative video of normal RBCs perfused through acellular collagen capillary-shaped channels at physiological hematocrit accumulating a significant amount before entering the capillary region and jetting and leading to significantly lower hematocrit into the downstream.

Movie S4. Representative video of normal RBCs stretching through capillaries (diameter, ~10 μm) when perfused at the single-cell scale.

Movie S5. Representative video of normal RBCs tumbling through capillaries (diameter, ~10 μm) when perfused at the single-cell scale.

Movie S6. Representative video of 2G2 IRBCs tumbling through capillaries (diameter, ~10 μm) when perfused at the single-cell scale.

Movie S7. Representative video of normal RBCs perfused through the capillaries at physiological hematocrit with no cell accumulation in the lumen.
Movie S8. Representative video of IT4VAR19 IRBCs perfused through the capillaries at physiological hematocrit accumulating a significant amount and blocking the capillary flow.
Movie S9. Representative video of trypsinized IT4VAR19 perfused through the capillaries showing a significant decrease in cell accumulation and not blocking the capillary flow.
Movie S10. Representative video of 2G2 IRBCs perfused through the capillaries at physiological hematocrit accumulating at postcapillary regions but not blocking the capillary flow.
References (*61*, *62*)

View/request a protocol for this paper from *Bio-protocol*.

REFERENCES AND NOTES

1. L. H. Miller, D. I. Baruch, K. Marsh, O. K. Doumbo, The pathogenic basis of malaria. *Nature* **415**, 673–679 (2002).
2. K. H. Merkel, P. L. Ginsberg, J. C. Parker Jr., M. J. Post, Cerebrovascular disease in sickle cell anemia: A clinical, pathological and radiological correlation. *Stroke* **9**, 45–52 (1978).
3. A. V. Buys, M. J. van Rooy, P. Soma, D. van Papendorp, B. Lipinski, E. Pretorius, Changes in red blood cell membrane structure in type 2 diabetes: A scanning electron and atomic force microscopy study. *Cardiovasc. Diabetol.* **12**, 25 (2013).
4. J. Chiodini, Apps from the World Health Organization - The World Malaria Report and more. *Travel Med. Infect. Dis.* **22**, 82–84 (2018).
5. N. J. White, G. D. Turner, N. P. Day, A. M. Dondorp, Lethal malaria: Marchiafava and Bignami were right. *J. Infect. Dis.* **208**, 192–198 (2013).
6. A. Kilejian, Characterization of a protein correlated with the production of knob-like protrusions on membranes of erythrocytes infected with *Plasmodium falciparum*. *Proc. Natl. Acad. Sci. U.S.A.* **76**, 4650–4653 (1979).
7. Y. Zhang, C. Huang, S. Kim, M. Golkaram, M. W. A. Dixon, L. Tilley, J. Li, S. Zhang, S. Suresh, Multiple stiffening effects of nanoscale knobs on human red blood cells infected with *Plasmodium falciparum* malaria parasite. *Proc. Natl. Acad. Sci. U.S.A.* **112**, 6068–6073 (2015).
8. D. I. Baruch, B. L. Pasloske, H. B. Singh, X. Bi, X. C. Ma, M. Feldman, T. F. Taraschi, R. J. Howard, Cloning the *P. falciparum* gene encoding PfEMP1, a malarial variant antigen and adherence receptor on the surface of parasitized human erythrocytes. *Cell* **82**, 77–87 (1995).
9. B. S. Crabb, B. M. Cooke, J. C. Reeder, R. F. Waller, S. R. Caruana, K. M. Davern, M. E. Wickham, G. V. Brown, R. L. Coppel, A. F. Cowman, Targeted gene disruption shows that knobs enable malaria-infected red cells to cytoadhere under physiological shear stress. *Cell* **89**, 287–296 (1997).
10. P. H. David, M. Hommel, L. H. Miller, I. J. Udeinya, L. D. Oligino, Parasite sequestration in *Plasmodium falciparum* malaria: Spleen and antibody modulation of cytoadherence of infected erythrocytes. *Proc. Natl. Acad. Sci. U.S.A.* **80**, 5075–5079 (1983).
11. A. M. Dondorp, R. Ruangveerayuth, K. T. Chotivanich, P. A. Kager, K. Silamut, B. J. Angus, M. R. Hardeman, A. M. Dondorp, N. J. White, J. Vreeken, Prognostic significance of reduced red blood cell deformability in severe falciparum malaria. *Am. J. Trop. Med. Hyg.* **57**, 507–511 (1997).
12. C. Raventos-Suarez, D. K. Kaul, F. Macaluso, R. L. Nagel, Membrane knobs are required for the microcirculatory obstruction induced by Plasmodium falciparum-infected erythrocytes. *Proc. Natl. Acad. Sci. U.S.A.* **82**, 3829–3833 (1985).
13. J. D. Smith, C. E. Chitnis, A. G. Craig, D. J. Roberts, D. E. Hudson-Taylor, D. S. Peterson, R. Pinches, C. I. Newbold, L. H. Miller, Switches in expression of Plasmodium falciparum var genes correlate with changes in antigenic and cytoadherent phenotypes of infected erythrocytes. *Cell* **82**, 101–110 (1995).
14. M. Bernabeu, J. D. Smith, EPCR and malaria severity: The center of a perfect storm. *Trends Parasitol.* **33**, 295–308 (2017).
15. A. M. Dondorp, C. I. Fanello, I. C. Hendriksen, E. Gomes, A. Seni, K. D. Chhaganlal, K. Bojang, R. Olaosebikan, N. Anunobi, K. Maitland, E. Kivaya, T. Agbenyega, S. B. Nguah, J. Evans, S. Gesase, C. Kahabuka, G. Mtove, B. Nadjm, J. Deen, J. Mwanga-Amumpaire, M. Nansumba, C. Karema, N. Umulisa, A. Uwimana, O. A. Mokuolu, O. T. Adedoyin, W. B. Johnson, A. K. Tshefu, M. A. Onyamboko, T. Sakulthaew, W. P. Ngum, K. Silamut, K. Stepniewska, C. J. Woodrow, D. Bethell, B. Wills, M. Oneko, T. E. Peto, L. von Seidlein, N. P. Day, N. J. White; AQUAMAT group, Artesunate versus quinine in the treatment of severe falciparum malaria in African children (AQUAMAT): An open-label, randomised trial. *Lancet* **376**, 1647–1657 (2010).
16. K. Dorovini-Zis, K. Schmidt, H. Huynh, W. Fu, R. O. Whitten, D. Milner, S. Kamiza, M. Molyneux, T. E. Taylor, The neuropathology of fatal cerebral malaria in malawian children. *Am. J. Pathol.* **178**, 2146–2158 (2011).
17. V. Barrera, I. J. C. MacCormick, G. Czanner, P. S. Hiscott, V. A. White, A. G. Craig, N. A. V. Beare, L. H. Culshaw, Y. Zheng, S. C. Biddolph, D. A. Milner, S. Kamiza, M. E. Molyneux, T. E. Taylor, S. P. Harding, Neurovascular sequestration in paediatric *P. falciparum* malaria is visible clinically in the retina. *ELife* **7**, e32208 (2018).
18. L. H. Miller, Distribution of mature trophozoites and schizonts of *Plasmodium falciparum* in the organs of *Aotus trivirgatus*, the night monkey. *Am. J. Trop. Med. Hyg.* **18**, 860–865 (1969).
19. R. Skalak, P. I. Branemark, Deformation of red blood cells in capillaries. *Science* **164**, 717–719 (1969).
20. J. P. Shelby, J. White, K. Ganesan, P. K. Rathod, D. T. Chiu, A microfluidic model for single-cell capillary obstruction by *Plasmodium falciparum*-infected erythrocytes. *Proc. Natl. Acad. Sci. U.S.A.* **100**, 14618–14622 (2003).
21. K. Tsukada, E. Sekizuka, C. Oshio, H. Minamitani, Direct measurement of erythrocyte deformability in diabetes mellitus with a transparent microchannel capillary model and high-speed video camera system. *Microvasc. Res.* **61**, 231–239 (2001).
22. J. M. Higgins, D. T. Eddington, S. N. Bhatia, L. Mahadevan, Sickle cell vasoocclusion and rescue in a microfluidic device. *Proc. Natl. Acad. Sci. U.S.A.* **104**, 20496–20500 (2007).
23. P. Gaehtgens, C. Duhrssen, K. H. Albrecht, Motion, deformation, and interaction of blood cells and plasma during flow through narrow capillary tubes. *Blood Cells* **6**, 799–817 (1980).
24. H. Noguchi, G. Gompper, Shape transitions of fluid vesicles and red blood cells in capillary flows. *Proc. Natl. Acad. Sci. U.S.A.* **102**, 14159–14164 (2005).
25. T. Herricks, K. B. Seydel, M. Molyneux, T. Taylor, P. K. Rathod, Estimating physical splenic filtration of *Plasmodium falciparum*-infected red blood cells in malaria patients. *Cell. Microbiol.* **14**, 1880–1891 (2012).
26. T. T. Keller, A. T. Mairuhu, M. D. de Kruif, S. K. Klein, V. E. Gerdes, H. ten Cate, D. P. Brandjes, M. Levi, E. van Gorp, Infections and endothelial cells. *Cardiovasc. Res.* **60**, 40–48 (2003).
27. O. Yalcin, V. P. Jani, P. C. Johnson, P. Cabrales, Implications enzymatic degradation of the endothelial glycocalyx on the microvascular hemodynamics and the arteriolar red cell free layer of the rat cremaster muscle. *Front. Physiol.* **9**, 168 (2018).
28. B. G. Yipp, S. Anand, T. Schollaardt, K. D. Patel, S. Looareesuwan, M. Ho, Synergism of multiple adhesion molecules in mediating cytoadherence of *Plasmodium falciparum*-infected erythrocytes to microvascular endothelial cells under flow. *Blood* **96**, 2292–2298 (2000).
29. M. R. Gillrie, M. Avril, A. J. Brazier, S. P. Davis, M. F. Stins, J. D. Smith, M. Ho, Diverse functional outcomes of *Plasmodium falciparum* ligation of EPCR: Potential implications for malarial pathogenesis. *Cell. Microbiol.* **17**, 1883–1899 (2015).
30. J. Storm, J. S. Jespersen, K. B. Seydel, T. Szestak, M. Mbewe, N. V. Chisala, P. Phula, C. W. Wang, T. E. Taylor, C. A. Moxon, T. Lavstsen, A. G. Craig, Cerebral malaria is associated with differential cytoadherence to brain endothelial cells. *EMBO Mol. Med.* **11**, e9164 (2019).
31. Y. Zheng, J. Chen, M. Craven, N. W. Choi, K. Totorica, A. Diaz-Santana, P. Kermani, B. Hempstead, C. Fischbach-Teschl, J. A. López, A. D. Stroock, In vitro microvessels for the study of angiogenesis and thrombosis. *Proc. Natl. Acad. Sci. U.S.A.* **109**, 9342–9347 (2012).
32. C. K. Arakawa, B. A. Badeau, Y. Zheng, C. A. DeForest, Multicellular vascularized engineered tissues through user-programmable biomaterial photodegradation. *Adv. Mater.* **29**, 1703156 (2017).
33. J. Escaned, A. Flores, P. García-Pavía, J. Segovia, J.. Jimenez, P. Aragoncillo, C. Salas, F. Alfonso, R. Hernández, D. J. Angiolillo, P. Jiménez-Quevedo, C. Bañuelos, L. Alonso-Pulpón, C. Macaya, Assessment of microcirculatory remodeling with intracoronary flow velocity and pressure measurements: Validation with endomyocardial sampling in cardiac allografts. *Circulation* **120**, 1561–1568 (2009).
34. A. G. Hudetz, Blood flow in the cerebral capillary network: A review emphasizing observations with intravital microscopy. *Microcirculation* **4**, 233–252 (1997).
35. T. W. Secomb, Blood flow in the microcirculation. *Annu. Rev. Fluid Mech.* **49**, 443–461 (2017).
36. D. Kleinfeld, P. P. Mitra, F. Helmchen, W. Denk, Fluctuations and stimulus-induced changes in blood flow observed in individual capillaries in layers 2 through 4 of rat neocortex. *Proc. Natl. Acad. Sci. U.S.A.* **95**, 15741–15746 (1998).
37. J. Mauer, S. Mendez, L. Lanotte, F. Nicoud, M. Abkarian, G. Gompper, D. A. Fedosov, Flow-induced transitions of red blood cell shapes under shear. *Phys. Rev. Lett.* **121**, 118103 (2018).
38. L. Lanotte, J. Mauer, S. Mendez, D. A. Fedosov, J. M. Fromental, V. Claveria, F. Nicoud, G. Gompper, M. Abkarian, Red cells' dynamic morphologies govern blood shear thinning under microcirculatory flow conditions. *Proc. Natl. Acad. Sci. U.S.A.* **113**, 13289–13294 (2016).
39. E. Hanssen, C. Knoechel, M. Dearnley, M. W. A. Dixon, M. le Gros, C. Larabell, L. Tilley, Soft x-ray microscopy analysis of cell volume and hemoglobin content in erythrocytes infected with asexual and sexual stages of Plasmodium falciparum. *J. Struct. Biol.* **177**, 224–232 (2012).
40. P. Horrocks, R. Pinches, Z. Christodoulou, S. A. Kyes, C. I. Newbold, Variable var transition rates underlie antigenic variation in malaria. *Proc. Natl. Acad. Sci. U.S.A.* **101**, 11129–11134 (2004).
41. B. G. Yipp, M. J. Hickey, G. Andonegui, A. G. Murray, S. Looareesuwan, P. Kubes, M. Ho, Differential roles of CD36, ICAM-1, and P-selectin in *Plasmodium falciparum* cytoadherence in vivo. *Microcirculation* **14**, 593–602 (2007).
42. H. W. Hou, A. A. S. Bhagat, A. G. Lin Chong, P. Mao, K. S. Wei Tan, J. Han, C. T. Lim, Deformability based cell margination—A simple microfluidic design for malaria-infected erythrocyte separation. *Lab Chip* **10**, 2605–2613 (2010).

43. Y. Imai, K. Nakaaki, H. Kondo, T. Ishikawa, C. Teck Lim, T. Yamaguchi, Margination of red blood cells infected by *Plasmodium falciparum* in a microvessel. *J. Biomech.* **44**, 1553–1558 (2011).
44. M. Avril, A. J. Brazier, M. Melcher, S. Sampath, J. D. Smith, DC8 and DC13 var genes associated with severe malaria bind avidly to diverse endothelial cells. *PLOS Pathog.* **9**, e1003430 (2013).
45. R. Jambou, V. Combes, M. J. Jambou, B. B. Weksler, P. O. Couraud, G. E. Grau, Plasmodium falciparum adhesion on human brain microvascular endothelial cells involves transmigration-like cup formation and induces opening of intercellular junctions. *PLOS Pathog.* **6**, e1001021 (2010).
46. C. L. Hutchings, A. Li, K. M. Fernandez, T. Fletcher, L. A. Jackson, J. B. Molloy, W. K. Jorgensen, C. T. Lim, B. M. Cooke, New insights into the altered adhesive and mechanical properties of red blood cells parasitized by Babesia bovis. *Mol. Microbiol.* **65**, 1092–1105 (2007).
47. S. G. Langreth, E. Peterson, Pathogenicity, stability, and immunogenicity of a knobless clone of *Plasmodium falciparum* in Colombian owl monkeys. *Infect. Immun.* **47**, 760–766 (1985).
48. F. K. Glenister, R. L. Coppel, A. F. Cowman, N. Mohandas, B. M. Cooke, Contribution of parasite proteins to altered mechanical properties of malaria-infected red blood cells. *Blood* **99**, 1060–1063 (2002).
49. L. Turner, T. Lavstsen, S. S. Berger, C. W. Wang, J. E. V. Petersen, M. Avril, A. J. Brazier, J. Freeth, J. S. Jespersen, M. A. Nielsen, P. Magistrado, J. Lusingu, J. D. Smith, M. K. Higgins, T. G. Theander, Severe malaria is associated with parasite binding to endothelial protein C receptor. *Nature* **498**, 502–505 (2013).
50. M. Bernabeu, C. Gunnarsson, M. Vishnyakova, C. C. Howard, R. J. Nagao, M. Avril, T. E. Taylor, K. B. Seydel, Y. Zheng, J. D. Smith, Binding heterogeneity of *Plasmodium falciparum* to engineered 3D brain microvessels is mediated by EPCR and ICAM-1. *MBio* **10**, e00420-19 (2019).
51. L. T. Chen, L. Weiss, The role of the sinus wall in the passage of erythrocytes through the spleen. *Blood* **41**, 529–537 (1973).
52. L. G. Rigat-Brugarolas, A. Elizalde-Torrent, M. Bernabeu, M. de Niz, L. Martin-Jaular, C. Fernandez-Becerra, A. Homs-Corbera, J. Samitier, H. A. del Portillo, A functional microengineered model of the human splenon-on-a-chip. *Lab Chip* **14**, 1715–1724 (2014).
53. C. P. Sanchez, C. Karathanasis, R. Sanchez, M. Cyrklaff, J. Jäger, B. Buchholz, U. S. Schwarz, M. Heilemann, M. Lanzer, Single-molecule imaging and quantification of the immune-variant adhesin VAR2CSA on knobs of *Plasmodium falciparum*-infected erythrocytes. *Commun. Biol.* **2**, 172 (2019).
54. J. Lou, R. Lucas, G. E. Grau, Pathogenesis of cerebral malaria: Recent experimental data and possible applications for humans. *Clin. Microbiol. Rev.* **14**, 810–820 (2001).
55. T. Lavstsen, L. Turner, F. Saguti, P. Magistrado, T. S. Rask, J. S. Jespersen, C. W. Wang, S. S. Berger, V. Baraka, A. M. Marquard, A. Seguin-Orlando, E. Willerslev, M. T. P. Gilbert, J. Lusingu, T. G. Theander, *Plasmodium falciparum* erythrocyte membrane protein 1 domain cassettes 8 and 13 are associated with severe malaria in children. *Proc. Natl. Acad. Sci. U.S.A.* **109**, E1791–E1800 (2012).
56. F. Duffy, M. Bernabeu, P. H. Babar, A. Kessler, C. W. Wang, M. Vaz, L. Chery, W. L. Mandala, S. J. Rogerson, T. E. Taylor, K. B. Seydel, T. Lavstsen, E. Gomes, K. Kim, J. Lusingu, P. K. Rathod, J. D. Aitchison, J. D. Smith, Meta-analysis of *Plasmodium falciparum var* signatures contributing to severe malaria in African children and Indian adults. *MBio* **10**, e00217-19 (2019).
57. K. A. Quadt, L. Barfod, D. Andersen, J. Bruun, B. Gyan, T. Hassenkam, M. F. Ofori, L. Hviid, The density of knobs on Plasmodium falciparum-infected erythrocytes depends on developmental age and varies among isolates. *PLOS ONE* **7**, e45658 (2012).
58. H. J. Lee, A. Georgiadou, M. Walther, D. Nwakanma, L. B. Stewart, M. Levin, T. D. Otto, D. J. Conway, L. J. Coin, A. J. Cunnington, Integrated pathogen load and dual transcriptome analysis of systemic host-pathogen interactions in severe malaria. *Sci. Transl. Med.* **10**, eaar3619 (2018).
59. M. Avril, A. K. Tripathi, A. J. Brazier, C. Andisi, J. H. Janes, V. L. Soma, D. J. Sullivan, P. C. Bull, M. F. Stins, J. D. Smith, A restricted subset of *var* genes mediates adherence of *Plasmodium falciparum*-infected erythrocytes to brain endothelial cells. *Proc. Natl. Acad. Sci. U.S.A.* **109**, E1782–E1790 (2012).
60. J. H. Janes, C. P. Wang, E. Levin-Edens, I. Vigan-Womas, M. Guillotte, M. Melcher, O. Mercereau-Puijalon, J. D. Smith, Investigating the host binding signature on the Plasmodium falciparum PfEMP1 protein family. *PLOS Pathog.* **7**, e1002032 (2011).
61. V. L. Cross, Y. Zheng, N. Won Choi, S. S. Verbridge, B. A. Sutermaster, L. J. Bonassar, C. Fischbach, A. D. Stroock, Dense type I collagen matrices that support cellular remodeling and microfabrication for studies of tumor angiogenesis and vasculogenesis in vitro. *Biomaterials* **31**, 8596–8607 (2010).
62. G. Ligresti, R. J. Nagao, J. Xue, Y. J. Choi, J. Xu, S. Ren, T. Aburatani, S. K. Anderson, J. W. MacDonald, T. K. Bammler, S. M. Schwartz, K. A. Muczynski, J. S. Duffield, J. Himmelfarb, Y. Zheng, A novel three-dimensional human peritubular microvascular system. *J. Am. Soc. Nephrol.* **27**, 2370–2381 (2016).

Acknowledgments: We acknowledge the Lynn and Mike Garvey Imaging Laboratory in the Institute of Stem Cell and Regenerative Medicine, the Nanotech User Facility, and the Flow Cytometry Facility, all at the University of Washington, and the Electron Microscope Facility in the Fred Hutchinson Cancer Research Institute. We thank R. Nagao for the helpful discussion and N. Sniadecki for sharing his microscope. We acknowledge the imaging and flow cytometry facility at the Seattle Children's Research Institute. **Funding:** This work is supported by the NIH R01 HL130488 (to J.D.S. and Y.Z.), R01HL141570, UG3TR002158, and UH2/UH3 DK107343 (to Y.Z.), and 2T32EB001650 and F30HL134298 (to C.A.); the NSF 1652141 and 1807398 (to C.A.D.); and the AHA postdoctoral fellowship (to M.B.). **Author contributions:** Y.Z. conceived the project. Y.Z., J.D.S., and C.A.D. supervised the project. C.A., C.G., C.H., M.B., J.D.S., and Y.Z. designed the experiments. C.A., C.G., C.H., and M.B. performed the experiments and data analysis with the assistance of K.P. and E.Y. All authors interpreted the data. C.A., C.G., J.D.S., and Y.Z. wrote the manuscript. All authors edited and approved the manuscript. **Competing interests:** The authors declare that they have no competing interests. **Data and materials availability:** All data needed to evaluate the conclusions in this paper are present in the paper and/or the Supplementary Materials. Additional data related to this paper may be requested from the corresponding author (yingzy@uw.edu).

Submitted 14 July 2019
Accepted 20 November 2019
Published 17 January 2020
10.1126/sciadv.aay7243

Citation: C. Arakawa, C. Gunnarsson, C. Howard, M. Bernabeu, K. Phong, E. Yang, C. A. DeForest, J. D. Smith, Y. Zheng, Biophysical and biomolecular interactions of malaria-infected erythrocytes in engineered human capillaries. *Sci. Adv.* **6**, eaay7243 (2020).

Biophysical and biomolecular interactions of malaria-infected erythrocytes in engineered human capillaries

Christopher Arakawa, Celina Gunnarsson, Caitlin Howard, Maria Bernabeu, Kiet Phong, Eric Yang, Cole A. DeForest, Joseph D. Smith and Ying Zheng

Sci Adv **6** (3), eaay7243.
DOI: 10.1126/sciadv.aay7243

Science Advances (ISSN 2375-2548) is published by the American Association for the Advancement of Science, 1200 New York Avenue NW, Washington, DC 20005. The title *Science Advances* is a registered trademark of AAAS.